Proceedings of the 11th ICPMG 2026
11th International Conference on Physical Modelling in Geotechnics
8-12 June 2026, Zurich, Switzerland

Bridge Foundation Instability under Climatic Extremes: Experimental and Numerical Insights into Driftwood and Seepage Impacts

A.S. Ali, Y. Nagoya, K. Isobe
Hokkaido University, Sapporo, Japan, aghashahali.syed.h6@elms.hokudai.ac.jp, nagoya.yutaka.g4@elms.hokudai.ac.jp, kisobe@eng.hokudai.ac.jp

Q. N. Pham
The University of Danang – University of Science and Technology, Danang, Viet Nam ngocquanggv@gmail.com

T. Hoshina
Sato Kogyo Ltd. Company, Tokyo, Japan, hoshina@satokogyo.co.jp

ABSTRACT: With recent shifts in global climate patterns, increased rainfall has become more frequent, posing significant challenges to road infrastructure. Bridges, critical links in national transport networks, have suffered structural damage due to the accumulation of sediment and driftwood at piers, which induces damming upstream and alters hydraulic behaviour. In this research, a series of physical model experiments, supported by rigid plastic finite element simulations, were conducted to evaluate the influence of waterhead differences generated by damming and the application of lateral forces simulating driftwood accumulation. The results revealed that the damming effect initiates upward seepage flow beneath the foundation, reducing effective stress and consequently the shear strength of the soil. Simultaneously, increased lateral forces caused by the girder being submerged in water due to the driftwood capture promote sliding and tilting of the pier. These deformations, in turn, exacerbate internal and external erosion and contribute to a brittle geotechnical failure of the foundation system. A method was proposed to evaluate this complex failure phenomenon, incorporating the combined effects of hydraulic head, debris loading, and progressive soil weakening through this research. The proposed equation captures the mechanisms as observed in the experiments, demonstrating significant loss of vertical and horizontal resistance. These findings highlight the need to consider the interplay between internal seepage-driven soil degradation and external driftwood-induced forces when assessing the stability of bridge foundations under extreme climatic and hydrological conditions.

1 INTRODUCTION

In recent years, bridge pier damage during torrential rains and abnormal water levels has increased, largely due to internal erosion and local scouring around foundations. When driftwood accumulates around piers and forms a dam-like obstruction, the resulting rise in water pressure intensifies seepage, further degrading foundation stability as shown in Figure 1 (Ren et al., 2024). However, an evaluation method that accounts for the reduction in bearing capacity caused by driftwood-induced damming has yet to be fully established.

Related studies (Mori & Sasaki, 2012; Takahashi et al., 2011; Badroddin & Chen, 2021; Guo et al., 2020; Kadono et al., 2020; Kong et al., 2017; Li et al., 2021; Maricar et al., 2020; Oudenbroek et al., 2018; Pregnolato et al., 2023) following the 2011 Tohoku Earthquake revealed that large hydraulic head differences, that in some severe cases would cause tilting of the girders and ultimately lead to the collapse of the entire bridge structures, combined with debris accumulation, triggered internal erosion and led to the failure of robust coastal and hydraulic structures. Subsequent physical model tests (Kasama et al., 2020) showed that sustained head differences produce strong seepage beneath foundations, causing horizontal loading and significant reductions in bearing capacity, which is often the governing failure under flooding conditions and cause of failure form any coastal and hydraulic structures.

Subsequent physical model studies investigating the influence of large and persistent hydraulic head differences revealed that these conditions could significantly affect foundation stability by generating intense seepage flow through and beneath the structure (Kasama et al., 2020). The primary mechanisms of failure were attributed to (i) horizontal static forces produced by hydraulic head variations between upstream and downstream sides, and (ii) a reduction in bearing capacity caused by seepage flow beneath the foundation. These interpretations were supported by observations that the non-seepage-induced horizontal bearing capacity (characterized by sliding-type failure) was considerably greater than the bearing capacity under seepage conditions.

Recent physical model tests by and Jones & Anastasopoulos (Jones & Anastasopoulos 2023) focused on determining the geotechnical failure mechanisms of caissons subjected to seepage flow. Their results demonstrated that severe internal erosion could lead to deep-seated foundation failure beneath caissons.

Figure 1. Case study of bridge damage caused by trapped driftwood.

While seepage-induced instability has been widely studied (Kasama et al., 2013; H. Takahashi et al., 2014; Zen et al., 2013), conventional analytical tools such as Hudson's (Hudson, 1959) and Isbash's equations Coastal Engineering Research Center (1977) do not capture the effects of drftwood-induced damming or tsunami-related seepage, both of which critically reduce foundation stability.

To address these gaps, the present study investigates bridge pier instability under seepage generated by driftwood damming. A predictive formula is proposed to estimate residual bearing capacity under varying hydraulic head differences, and a V–H limit load space is developed based on experimental observations. The framework incorporates hydraulic gradients, soil properties, and river-induced lateral loads. Validation is conducted through hydraulic model tests and numerical simulations, providing new insights for designing and assessing bridge foundations subjected to seepage-induced instability.

2 METHODOLOGY

This study specifically focuses on the effect of seepage forces on bearing capacity induced by the water level difference between the upstream and downstream sides of a bridge pier when the river channel is obstructed by accumulated driftwood. To isolate this mechanism, a cross-section along the bridge axis was considered. The complex multi-physics problem is decomposed into two manageable components: (1) scaled physical modelling of the bridge pier with the spread foundation, and (2) hybrid numerical simulations that support the physical model results and enable an extensive parametric investigation.

2.1 Physical Modelling

A small-scale bridge pier model was constructed at a geometric scale of 1/37 using aluminium, which ensures uniform mechanical interaction with sand (Jones & Anastasopoulos, 2022). The model measured 245 × 50 × 200 mm (L × W × H) as shown in Figure 2(a) and was embedded to a depth of 20 mm.

This study focuses on a spread foundation constructed on gravelly riverbed ground, assuming ground conditions that provide sufficient shear strength to function as a bearing layer while also exhibiting high permeability. To reproduce these assumed ground conditions in a gravity field model test, silica sand No. 7 was selected as the model ground material, with reference to Kadono et al. (2020).

The model ground consisted of Silica Sand No. 7, prepared by air pluviation to achieve relative densities of 40% and 80%, representing loose and dense states. The sand bed, with a final height of 300 mm, was constructed in twelve 25 mm layers, with density controlled through sand mass and layer thickness monitored by a laser displacement sensor The soil properties are shown in Table 1.

A 2.5 mm gap was kept between the model and tank walls to avoid constraint effects. After placement in the test tank, bentonite was applied at the four corners of the pier to act as waterproofing seals and minimize sidewall friction as shown in Figure 2(b).

The soil bed was fully saturated following the procedure of Mehdizadeh et al. (Mehdizadeh et al. 2021) and left to equilibrate for at least 12 hours as shown in Figure 3(a), to attain ground saturation. Seepage flow was induced by adjusting upstream and downstream water levels, maintaining the downstream level at least 2 cm lower as shown in Figure 3(b). Multiple hydraulic head differences were tested, where a series of attained heads on the upstream and downstream sides are listed in Table 2.

Vertical loading was applied using a load cell, and displacement response was recorded through displacement gauge, as shown in Figure 4. The resulting load-displacement curves provided the basis for evaluating foundation behaviour under seepage-induced hydraulic gradients.

Table 1. Model ground parameters using silica sand #7.

Properties	Values
Relative density *Dr* (%)	40 – 80
Cohesion *c* (kPa)	0
Shear resistance angle ϕ (deg.)	35 – 40
Unit weight γ_d (kN/m^3)	13.5 – 14.9

Table 2. Experimental conditions.

Properties	Values
Upstream water level H_1 (mm)	0 – 120
Downstream water level H_2 (mm)	0 – 80
Water lever difference (mm)	0 – 100
Hydraulic gradient i	0 – 1.1
Loading height from G.L. (m)	200
Loading angle θ (deg.)	0

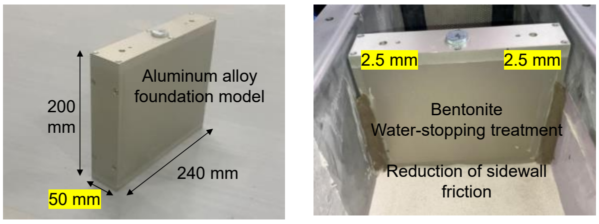

(a) Model dimensions. *(b) Waterproofing seals.*

Figure 2 (a) Model pier. (b) Use of Bentonite which acts as a waterproofing seal, between the upstream and downstream sides.

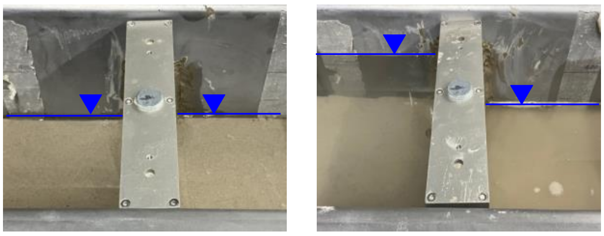

(a) Saturation phase. *(b) Testing phase.*

Figure 3 (a) Water level during the soil saturation phase of the experiment. (b) Maintained hydraulic head difference during the testing phase.

2.2 Numerical Modelling

The hybrid analysis method cooperating seepage analysis and rigid plastic FEA analysis used in this research is shown in Figure 5.

Initially, a seepage finite element analysis was conducted to quantify the pore water pressure variations in the ground caused by river-driftwood damming. Following the seepage analysis, the degree of saturation and pore water pressure distribution were incorporated into the subsequent Rigid Plastic Finite Element Method (RPFEM) originally developed by Tamura (Tamura et al., 1987) and later enhanced by Nguyen et al. (Nguyen et al., 2016).

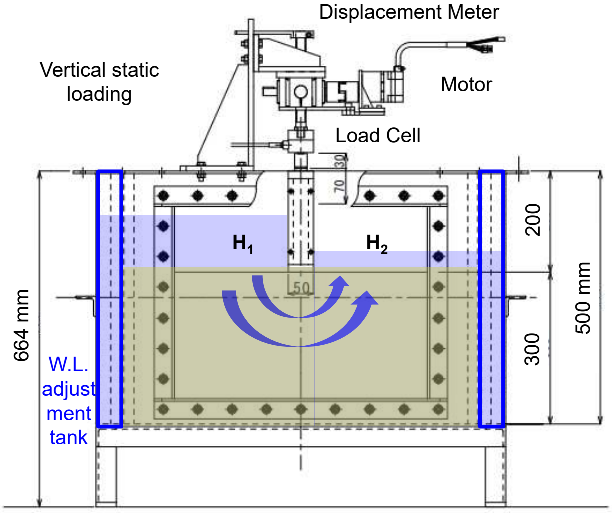

Figure 4 Schematic Diagram for Soil tank, model pier and loading device.

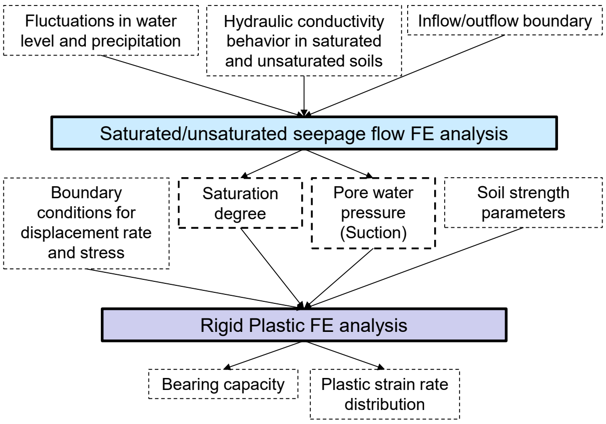

Figure 5 Hybrid analysis method cooperating seepage analysis and rigid plastic FEA analysis.

A rigid pier on a shallow footing placed over a flat, homogeneous ground was modelled, as illustrated in Figure 6. The prototype-scale parameters adopted in the analysis are summarized in Tables 3 and 4.

The RPFEM, employing a rigid-plastic constitutive model with the Drucker-Prager yield criterion, requires only a limited number of parameters and determines the limit load without assuming any specific failure mechanism, which is one of its primary advantages.

Accordingly, the Drucker–Prager yield criterion is adopted under plane-strain conditions with an associated flow rule. The Drucker–Prager yield function is expressed as follows, shown as Eq. (1):

$$f(\boldsymbol{\sigma}') = \omega I_1 + \sqrt{J_2} - \psi = 0 \qquad (1)$$

$$\omega = \frac{\tan\phi}{\sqrt{9+12\tan^2\phi}} \tag{2}$$

$$\psi = \frac{3c}{\sqrt{9+12\tan^2\phi}} \tag{3}$$

where, $I_1 = \mathrm{tr}(\boldsymbol{\sigma}')$ is the first invariant of effective stress tensor $\boldsymbol{\sigma}'$, $J_2 = \frac{1}{2}\mathbf{s}:\mathbf{s}$ is the second invariant of deviatoric stress tensor $\mathbf{s}$, ω and ψ are material constants related to the soil friction angle ϕ and cohesion c, respectively. These parameters are expressed under plane strain condition as shown in Eqs. (2) and (3).

The volumetric strain rate $\dot{\varepsilon}_v$ is expressed as follows in Eq. (4). The strain rate $\dot{\boldsymbol{\varepsilon}}$, assumed to be purely plastic $\dot{\boldsymbol{\varepsilon}}^p$, must satisfy the volumetric constraint condition defined by Eq. (5), as follows:

$$\dot{\varepsilon}_v = \mathrm{tr}(\dot{\boldsymbol{\varepsilon}}) = \mathrm{tr}\left(\lambda\frac{\partial f(\boldsymbol{\sigma}')}{\partial\boldsymbol{\sigma}'}\right) = tr\left(\lambda\left(\omega\mathbf{I} + \frac{\mathbf{s}}{2\sqrt{J_2}}\right)\right) = \frac{3\omega}{\sqrt{3\omega^2+\frac{1}{2}}}\dot{e} \tag{4}$$

$$h(\dot{\boldsymbol{\varepsilon}}) = \dot{\varepsilon}_v - \frac{3\omega}{\sqrt{3\omega^2+\frac{1}{2}}}\dot{e} = 0 \tag{5}$$

where, λ and $\mathbf{I}$ denote plastic strain rate multiplier and the unit tensor, respectively. The norm of the strain rate $\dot{e}$ is defined as $\dot{e} = \sqrt{\dot{\boldsymbol{\varepsilon}}^p : \dot{\boldsymbol{\varepsilon}}^p}$.

The stress and strain rate relationship for the Drucker-Prager yield function is expressed with the use of penalty constant κ for the dilation property of plastic strain rate, as demonstrated in Eq. (6). Any admissible strain rate compatible with the Drucker–Prager yield criterion is further required to satisfy the kinematic constraint expressed by Eq. (5).

$$\boldsymbol{\sigma}' = \boldsymbol{\sigma}'^{(1)} + \boldsymbol{\sigma}'^{(2)} = \frac{\psi}{\sqrt{3\omega^2+\frac{1}{2}}}\frac{\dot{\boldsymbol{\varepsilon}}}{\dot{e}} + \eta\frac{\partial h(\dot{\boldsymbol{\varepsilon}})}{\partial\dot{\boldsymbol{\varepsilon}}} = \frac{\psi}{\sqrt{3\omega^2+\frac{1}{2}}}\frac{\dot{\boldsymbol{\varepsilon}}}{\dot{e}} + \eta\left\{\mathbf{I} - \frac{3\omega}{\sqrt{3\omega^2+1/2}}\frac{\dot{\boldsymbol{\varepsilon}}}{\dot{e}}\right\} = \frac{\psi}{\sqrt{3\omega^2+1/2}}\frac{\dot{\boldsymbol{\varepsilon}}}{\dot{e}} + \kappa(\dot{\varepsilon}_v - \beta\dot{e})\left(\mathbf{I} - \frac{3\omega}{\sqrt{3\omega^2+1/2}}\frac{\dot{\boldsymbol{\varepsilon}}}{\dot{e}}\right) \tag{6}$$

where, $\boldsymbol{\sigma}'^{(1)}$ is a determinate effective stress component governed by the yield function and $\boldsymbol{\sigma}'^{(2)}$ is an indeterminate effective stress component aligned with the yield surface. The indeterminate stress parameter η is resolved through solution of the boundary value problem.

The distribution of the strain-rate norm within the soil–structure system provides insight into the failure pattern. A small norm value corresponds to rigid-body behavior, which cannot be properly described by conventional plastic constitutive equations. In the numerical analysis, a small threshold value, $\dot{e}_0$, is introduced to represent rigid-body motion. When the computed norm of the plastic strain rate $\dot{e}$ falls below $\dot{e}_0$, it is replaced by $\dot{e}_0$. This prevents division by zero in the constitutive formulation and ensures numerical stability in regions exhibiting rigid-body behavior. Although this approach is a well-known numerical technique, its physical interpretation can be viewed as a reduction of the yield surface size, forcing the stress state in the rigid-body region to satisfy a modified yield function. The size of this modified yield surface is governed by the relative magnitude of the computed plastic strain-rate norm $\dot{e}$ and the prescribed threshold value $\dot{e}_0$.

The rigid–plastic constitutive model as shown in Eq. (6) is coupled with the force equilibrium (virtual work) equation as shown in Eq. (7) to obtain an equivalent analysis of the upper bound theorem for plasticity, explicitly accounting for the pore water pressure distribution u_w, which is obtained in advance from seepage flow analysis under varying water level conditions.

$$\int_V \boldsymbol{\sigma}' : \delta\dot{\boldsymbol{\varepsilon}}dV = \rho\int_{S_1}\mathbf{T_1} : \delta\dot{\mathbf{u}}dS_1 + \int_{S_2}\mathbf{T_2} : \delta\dot{\mathbf{u}}S_2 + \int_V \mathbf{X} : \delta\dot{\mathbf{u}}dV - u_w\int_V \mathbf{I} : \delta\dot{\boldsymbol{\varepsilon}}dV \tag{7}$$

$$\rho = -\mu\left(\int_{S_1}\mathbf{T_1} : \delta\dot{\mathbf{u}}dS_1 - 1\right) \tag{8}$$

In this formulation, ρ is the load factor, $\mathbf{T_1}$ represents the external load components (V–H–M) acting on boundary S_1, $\mathbf{T_2}$ is the constant force induced by hydrostatic pressure acting on boundary S_2, $\dot{\mathbf{u}}$ is the displacement rate, $\mathbf{X}$ denotes body forces due to self-weight and V is the analysis domain.

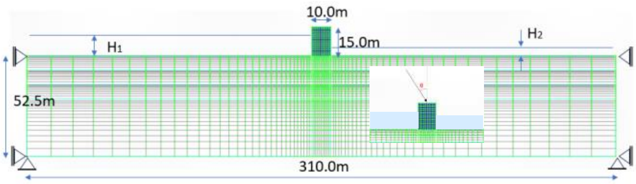

Figure 6 Prototype RPFEM pier geometry with assigned boundary conditions and variable mesh densities to balance computational efficiency and accuracy.

Table 3. Prototype Model geometry parameters and analytical conditions.

Properties	Values
Pier Height H (m)	15
Footing width B (m)	10
Embedment Depth D_f (m)	0, 2
Upstream water level H_1 (m)	5
Downstream water level H_2 (m)	4 – 5
Water lever difference W.L.D. (m)	0 – 1
Hydraulic gradient i	0 – 0.1
Loading height from G.L. (m)	0, 5, 10, 15
Loading angle θ (deg.)	0 – 40

Table 4. Bearing capacity analysis parameters.

Properties	Ground	Foundation
Cohesion c (kPa)	1	50000
Shear resistance angle ϕ (deg.)	30	0
Unit weight γ_{sat} (kN/m^3)	17.5	0

3 RESULTS

3.1 Influence of Hydraulic Gradient on the Vertical Bearing Capacity

Figures 7 and 8 illustrate the vertical load – settlement curve for D_r = 80%, 40% with an embedment depth of D_f = 20 mm, respectively. Vertical loading tests were performed while changing the water level difference (the upstream water level H_1 - the downstream water level H_2). A benchmark reference case V_{ult} was obtained by the case without the water level difference, corresponding to zero hydraulic head difference ($H_1 – H_2$ = 0 mm) across the footing, and was used as the basis for all comparisons. If a clear peak load was observed before the settlement reached 10% of the foundation width, the peak load was defined as the ultimate bearing capacity. If no distinct peak load was identified, the load corresponding to a settlement of 10% of the foundation width was defined as the ultimate bearing capacity. From these results, a more gradual reduction in the ultimate bearing capacity was observed under dense ground conditions due to the increase in difference of the water level.

Figure 9 shows the relationship between the hydraulic gradient and the reduction ratio of vertical bearing capacity obtained from both physical and numerical modelling, where the hydraulic gradient is normalized by the critical hydraulic gradient i_c. The results exhibit a sharp decrease in ultimate load, highlighting the significant influence of upward seepage flow. Based on these results, a trend equation was proposed using logarithmic regression to approximate the observed behavior as a function of the normalized hydraulic gradient i, as shown in Eq. (9), although some variability remains (the coefficient of determination is R^2 = 0.52).

$$V^* = V_{ult} e^{-1.26i/i_c} \tag{9}$$

where, V_{ult} is pure vertical bearing capacity without seepage force, V^* is pure vertical bearing capacity with seepage force, i_c is critical hydraulic gradient.

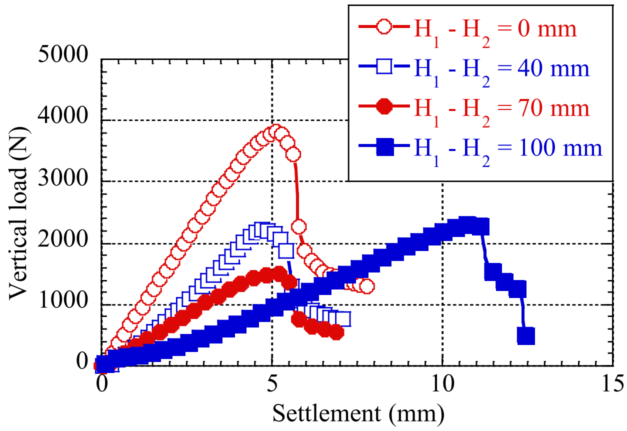

Figure 7 Vertical load – settlement curve for D_r = 80%.

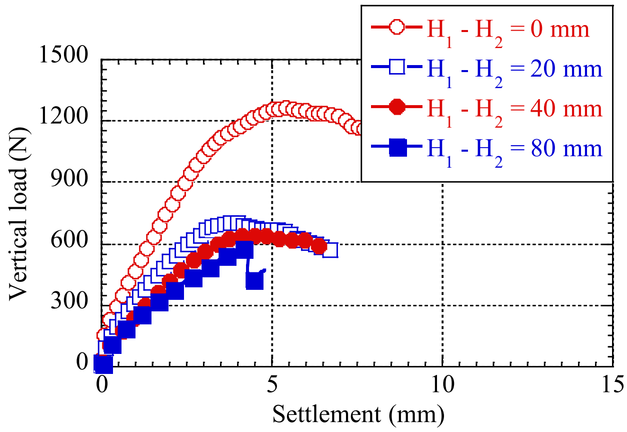

Figure 8 Vertical load – settlement curve for D_r = 40%.

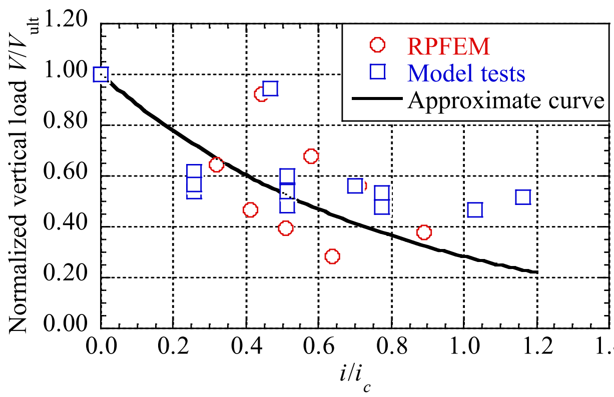

Figure 9 Variation of the normalized vertical bearing capacity with the increasing hydraulic gradient i/i_c.

3.2 Influence of Internal Seepage and Embedment Depth on Limit Load Space

Figures 10 and 11 show the limit load space obtained based on RPFEM for the cases with and without any embedment depth. According to these figures, the limit load space extends due to the embedment effect, which includes surcharge pressure and the shear strength of the ground beneath the foundation base. While seepage forces due to water level difference between upstream H_1 and downstream H_2 cause the limit load space to contract in both cases, the degree of this reduction varies with the embedment depth. Furthermore, when the difference in water levels is significant, the embedment effect on vertical bearing capacity is nearly nullified. However, the effect on horizontal bearing capacity remains evident.

Figure 12 shows the representative deformation mode for the case with loading angle of 10 deg. and 30 deg. From the figures, it can be observed that changes in the loading angle result in a corresponding shift in the failure mode of the bridge pier foundation, including reductions in bearing capacity as well as transitions between sliding and overturning. Although not shown here due to space constraints, additional analyses confirm that under coupled loading, where horizontal and moment loads are applied simultaneously at varying loading heights, the limit load envelope progressively contracts. As the loading angle increases together with the coupled horizontal load, the causes the system to approach its moment capacity, causing overturning type failure to emerge as the dominant failure mode.

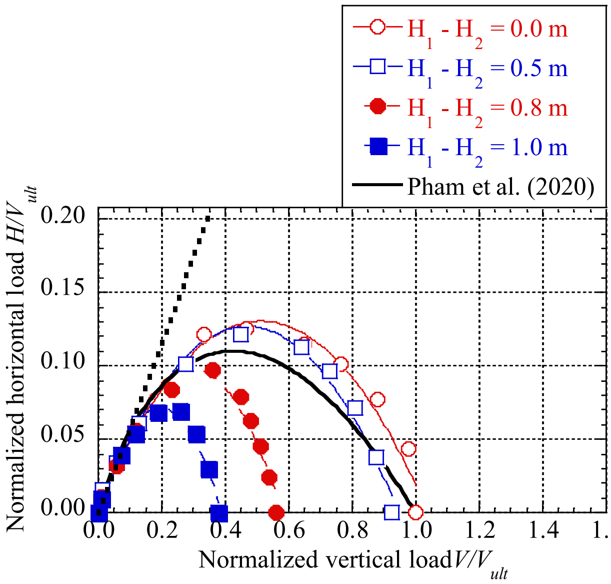

Figure 10. Limit load space (V-H plane) obtained for unembedded spread foundations (D_f = 0.0 m).

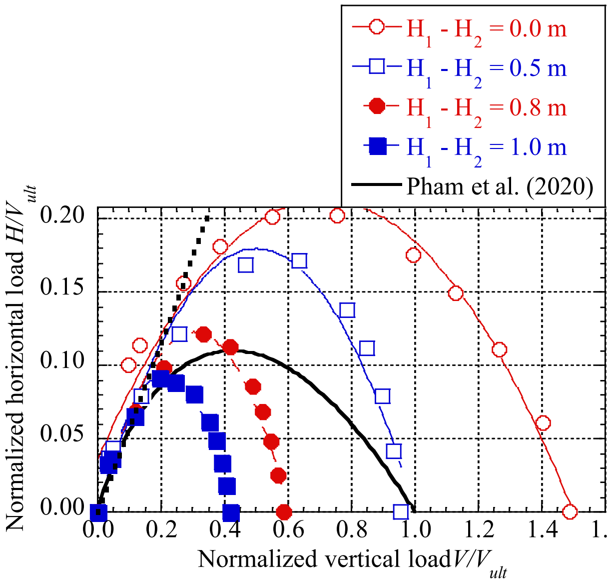

Figure 11. Limit load space (V-H plane) obtained for embedded spread foundations (D_f = 2.0 m).

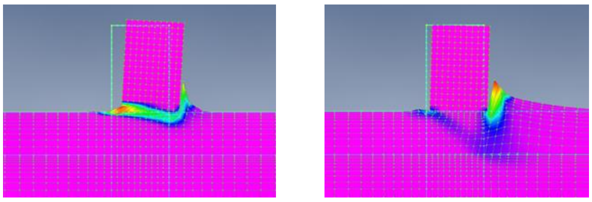

Figure 12. Differences in failure modes due to differences in loading angle: (left) 30° sliding mode, (right) 10° bearing failure.

4 STABILITY EVALUATION METHOD

Based on these obtained results, the following method for evaluating the stability of bridge pier foundations in the event of damming caused by driftwood accumulation is proposed as shown in Figures 13 and 14.

1) With reference to Pham et al. (Pham et al. 2020) and Eq. (9), a limit load space that takes into account seepage force is formulated by utilizing Eq. (10) and Eq (11).
2) The allowable bearing capacity is defined as the ultimate capacity under non-damming conditions divided by the safety factor F_s, and is assumed to correspond to the dead load acting on the foundation.
3) The cross section of the bearing surface in H-M plane is extracted (taking into account the effects of the foundation width and pier width along the bridge axis direction) as shown in Eq. (12).
4) A curve representing the cariation in H/V_{ult} - M/BV_{ult} due to a rise in river water level is obtained, taking into account the water level difference.
5) When any combination of a combined external force intersects and crosses the bearing capacity

curve formulated (and optionally the effect of girder flooding can be considered), it is determined that the pier foundation has now become unstable.

$$\frac{H_0}{V_{ult}} = \frac{tan\phi}{0.76}\frac{V}{V_{ult}}\left[1-\left(\frac{V}{V^*}\right)^{\frac{1}{(1.7tan\phi+0.4)^2}}\right] \quad (10)$$

$$\frac{M_0}{V_{ult}} = 0.55\frac{V}{V_{ult}}\left[1-\left(\frac{V}{V^*}\right)^{0.49}\right] \quad (11)$$

$$\left(\frac{H}{H_0}\right)^2+\left(\frac{M}{M_0}\right)^2+2C\left(\frac{H}{H_0}\right)\left(\frac{M}{M_0}\right)=\left(\frac{L_f}{L_p}\right) \quad (12)$$

where, H_0 is the ultimate horizontal load against allowable bearing capacity V_{ult}/F_s, M_0 is ultimate moment against allowable bearing capacity V_{ult}/F_s, L_f is the foundation width, L_p is the pier width, C is the fitting parameter.

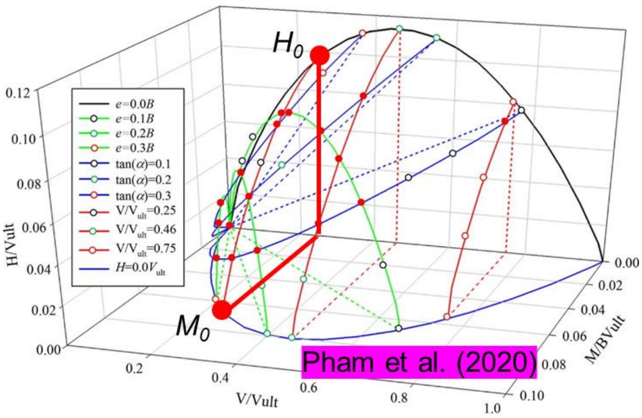

Figure 13. Limit load space based on Pham et al. (2020).

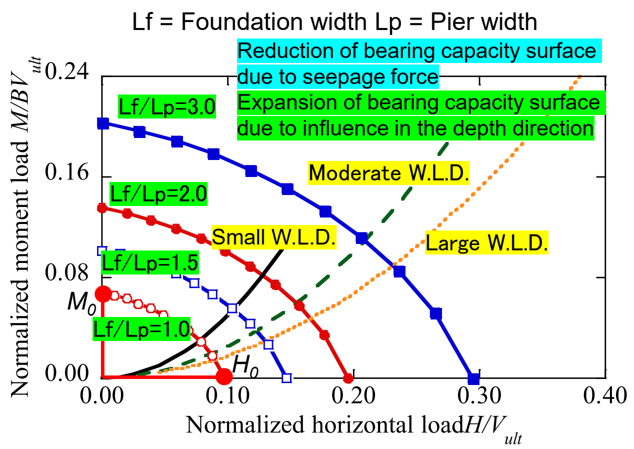

Figure 14. Proposed stability evaluation method concept.

5 CONCLUSIONS

This study investigated the bearing capacity of shallow bridge pier foundations affected by driftwood accumulation through numerical simulations supplemented by physical modelling. The results revealed that seepage flow plays a critical role in the degradation of bearing capacity. Moreover, the seepage force generated by the development of hydraulic head can displace finer particles within the soil matrix, creating voids as the soil is mobilized from its original position and leaving cavities behind. This process leads to a significant loss of vertical bearing capacity.

Based on these findings, a stability evaluation method was proposed that accounts for both the reduction in ground bearing capacity and the sudden increase in external forces caused by the damming effect associated with driftwood accumulation and obstruction at the pier during flooding events. The proposed approach demonstrates the potential to explain the brittle failure mechanisms observed in actual bridge pier foundations.

The estimation method will be further developed and generalized in future work to incorporate a broader range of parameters and scenarios. This advancement is expected to support the development of a limit load framework, enabling engineers to better predict bearing capacity loss following extreme rainfall or flooding events.

ACKNOWLEDGEMENTS

This study was financially supported, for which the authors are grateful, by the River Fund of The River Foundation, Japan.

REFERENCES

Badroddin, M., & Chen, Z. (2021). Lifetime Resilience Measurement of River-Crossing Bridges with Scour Countermeasures under Multiple Hazards. Journal of Engineering Mechanics, 147(9). https://doi.org/10.1061/(ASCE)EM.1943-7889.0001951

Coastal Engineering Research Center. (1977). Shore protection manual. US Army coastal engineering research center.

Guo, X., Zhang, C., & Chen, Z. (2020). Nonlinear Dynamic Response and Assessment of Bridges under Barge Impact with Scour Depth Effects. Journal of Performance of Constructed Facilities, 34(4). https://doi.org/10.1061/(ASCE)CF.1943-5509.0001467

Hudson, R. Y. (1959). Laboratory Investigation of Rubble-Mound Breakwaters. Journal of the Waterways and Harbors Division, 85(3), 93–121. https://doi.org/10.1061/JWHEAU.0000142

Jones, L., & Anastasopoulos, I. (2022). Breakwater subjected to tsunami–impact: Physical modelling of geotechnical phenomena. Soil Dynamics and

Earthquake Engineering, 159, 107344. https://doi.org/10.1016/j.soildyn.2022.107344

Jones, L., & Anastasopoulos, I. (2023). Bearing Capacity of Breakwater Subjected to Tsunami-Induced Scour. Journal of Geotechnical and Geoenvironmental Engineering, 149(6). https://doi.org/10.1061/JGGEFK.GTENG-11142

Kadono, T., Okazaki, S., Kabeyama, Y., & Matsui, T. (2020). Effect of Angle between Pier and Center of River Flow on Local Scouring around the Bridge Pier. Water, 12(11), 3192. https://doi.org/10.3390/w12113192

Kasama, K., Zen, K., & Kasugai, Y. (2013). Model experiment for the instability of caisson-type composite breakwater under tsunami condition. Journal of Japan Society of Civil Engineers, Ser. B2 (Coastal Engineering), 69(2), I_966-I_970. https://doi.org/10.2208/kaigan.69.I_966

Kasama, K., Zen, K., Nakagawa, Y., & Furukawa, Z. (2020). Instability evaluation of rubble mound for breakwaters subjected to tsunami-induced overflow and seepage flow. Soils and Foundations, 60(6), 1532–1545. https://doi.org/10.1016/j.sandf.2020.10.006

Kong, X., Cai, C. S., Hu, J. X., Xiong, W., & Peng, H. (2017). Field Application of an Innovative Bridge Scour Monitoring System with Fiber Bragg Grating Sensors. Journal of Aerospace Engineering, 30(2). https://doi.org/10.1061/(ASCE)AS.1943-5525.0000654

Li, Z., Tang, F., Chen, Y., Hu, X., Chen, G., & Tang, Y. (2021). Field experiment and numerical verification of the local scour depth of bridge pier with two smart rocks. Engineering Structures, 249, 113345. https://doi.org/10.1016/j.engstruct.2021.113345

Maricar, M. F., Maricar, F., Lopa, R. T., & Hashimoto, H. (2020). Flume experiments on log accumulation at the bridge with pier and without pier. IOP Conference Series: Earth and Environmental Science, 419(1), 012124. https://doi.org/10.1088/1755-1315/419/1/012124

Mehdizadeh, A., Disfani, M. M., & Shire, T. (2021). Post-erosion mechanical response of internally unstable soil of varying size and flow regime. Canadian Geotechnical Journal, 58(4), 531–539. https://doi.org/10.1139/cgj-2019-0790

Mori, N., & Sasaki, J. (2012). Nationwide Post Event Survey and Analysis of the 2011 Tohoku Earthquake Tsunami. Coastal Engineering in Japan, 54, 1250001.

Nguyen, D. L., Ohtsuka, S., Hoshina, T., & Isobe, K. (2016). Discussion on size effect of footing in ultimate bearing capacity of sandy soil using rigid plastic finite element method. Soils and Foundations, 56(1), 93–103. https://doi.org/10.1016/j.sandf.2016.01.007

Oudenbroek, K., Naderi, N., Bricker, J. D., Yang, Y., Van der Veen, C., Uijttewaal, W., Moriguchi, S., & Jonkman, S. N. (2018). Hydrodynamic and Debris-Damming Failure of Bridge Decks and Piers in Steady Flow. Geosciences, 8(11), 409. https://doi.org/10.3390/geosciences8110409

Pham, Q. N., Ohtsuka, S., Isobe, K., & Fukumoto, Y. (2020). Limit load space of rigid footing under eccentrically inclined load. Soils and Foundations, 60(4), 811–824. https://doi.org/10.1016/j.sandf.2020.05.004

Pregnolato, M., Giordano, P. F., Prendergast, L. J., Vardanega, P. J., & Limongelli, M. P. (2023). Comparison of risk-based methods for bridge scour management. Sustainable and Resilient Infrastructure, 8(5), 514–531.
https://doi.org/10.1080/23789689.2023.2175141

Ren, F., Isobe, K., & Ando, M. (2024). Risk Assessment of Bridge Damage Due to Heavy Rainfall Considering Landslide Risk and Driftwood Generation Potential Using Convolutional Neural Networks and Conventional Machine Learning. Water, 16(23), 3471. https://doi.org/10.3390/w16233471

Takahashi, H., Sassa, S., Morikawa, Y., Takano, D., & Maruyama, K. (2014). Stability of caisson-type breakwater foundation under tsunami-induced seepage. Soils and Foundations, 54(4), 789–805. https://doi.org/10.1016/j.sandf.2014.07.002

Takahashi, S., Toda, K., Kikuchi, Y., Sugano, T., Kuriyama, Y., & Yamazaki, H. (2011). Urgent survey for 2011 great east japan earthquake and tsunami disaster in ports and coasts. Technical Note of the Port and Airport Research Institute, 1–200.

Tamura, T., Kobayashi, S., & Sumi, T. (1987a). Rigid-Plastic Finite Element Method for Frictional Materials. *Soils and Foundations*, *27*(3), 1–12. https://doi.org/10.3208/sandf1972.27.3_1

Tamura, T., Kobayashi, S., & Sumi, T. (1987b). Rigid-Plastic Finite Element Method for Frictional Materials. *Soils and Foundations*, *27*(3), 1–12. https://doi.org/10.3208/sandf1972.27.3_1

Zen, K., Kasama, K., Kasugai, Y., & Dong, S. (2013). Failure of Rubble Mound Beneath Caisson due to Earthquake-Induced Tsunami. Volume 6: Polar and Arctic Sciences and Technology; Offshore Geotechnics; Petroleum Technology Symposium. https://doi.org/10.1115/OMAE2013-10059